



Article

# Exploring the Effects of the Interaction of Carbon and MoS<sub>2</sub> Catalyst on CO<sub>2</sub> Hydrogenation to Methanol

Pingping Cui, Ruyu Sun, Linfei Xiao \* and Wei Wu \*

National Center for International Research on Catalytic Technology, Key Laboratory of Chemical Engineering Process & Technology for High-Efficiency Conversion, College of Heilongjiang Province, School of Chemistry and Material Sciences, Heilongjiang University, Harbin 150080, China; c2191131pp@163.com (P.C.); sry1999sun@163.com (R.S.)

\* Correspondence: xiaolf@hlju.edu.cn (L.X.); wuwei@hlju.edu.cn (W.W.)

**Abstract:** Hydrogenation of CO<sub>2</sub> to form methanol utilizing green hydrogen is a promising route to realizing carbon neutrality. However, the development of catalyst with high activity and selectivity to methanol from the CO<sub>2</sub> hydrogenation is still a challenge due to the chemical inertness of CO<sub>2</sub> and its characteristics of multi-path conversion. Herein, a series of highly active carbon-confining molybdenum sulfide (MoS<sub>2</sub>@C) catalysts were prepared by the in-situ pyrolysis method. In comparison with the bulk MoS<sub>2</sub> and MoS<sub>2</sub>/C, the stronger interaction between MoS<sub>2</sub> and the carbon layer was clearly generated. Under the optimized reaction conditions, MoS<sub>2</sub>@C showed better catalytic performance and long-term stability. The MoS<sub>2</sub>@C catalyst could sustain around 32.4% conversion of CO<sub>2</sub> with 94.8% selectivity of MeOH for at least 150 h.

**Keywords:** MoS<sub>2</sub>@C; carbon dioxide; hydrogenation; methanol



**Citation:** Cui, P.; Sun, R.; Xiao, L.; Wu, W. Exploring the Effects of the Interaction of Carbon and MoS<sub>2</sub> Catalyst on CO<sub>2</sub> Hydrogenation to Methanol. *Int. J. Mol. Sci.* **2022**, *23*, 5220. <https://doi.org/10.3390/ijms23095220>

Academic Editor: Luisa Margarida Martins

Received: 15 April 2022

Accepted: 5 May 2022

Published: 7 May 2022

**Publisher's Note:** MDPI stays neutral with regard to jurisdictional claims in published maps and institutional affiliations.



**Copyright:** © 2022 by the authors. Licensee MDPI, Basel, Switzerland. This article is an open access article distributed under the terms and conditions of the Creative Commons Attribution (CC BY) license (<https://creativecommons.org/licenses/by/4.0/>).

## 1. Introduction

Carbon dioxide is one of the important greenhouse gases contributing to global warming, glacial melting, sea-level rise, ocean acidification, and hypercapnia [1,2]. While CO<sub>2</sub> is also an inexpensive, abundant, sustainable, and renewable C1 resource [3,4], it can be captured and utilized in a rational way to form high value-added chemicals, such as carbonate, methanol, formic acid, olefins, aromatics, and so on [5,6]. CO<sub>2</sub> conversion to MeOH is the most direct route for synthesizing oxygenated compounds and has received great interest [7–9]. As a feedstock, methanol can be used as a precursor for synthesizing aromatics and low olefins; moreover, it is also considered to be a green hydrogen carrier and is used as a fuel additive and fuel substitute directly [10]. Although the synthesis of MeOH from CO<sub>2</sub> and H<sub>2</sub> is exothermic, CO<sub>2</sub> conversion to MeOH is kinetically limited at low temperatures and thermodynamically limited at high temperatures. Due to a high activation energy barrier for the cleavage of the C-O bonds in CO<sub>2</sub>, which clearly results in a chief challenge to developing effective catalysts for the synthesis of methanol from CO<sub>2</sub> at a low temperature.

Until now, there are numerous endeavors on different catalyst systems to address CO<sub>2</sub> hydrogenation to methanol, such as Cu-based catalysts [11–13], precious metal catalysts [14–18], In<sub>2</sub>O<sub>3</sub>-based catalysts [19–21], solid solution catalysts [22–24], and so on. Among these catalysts, the Cu/ZnO/Al<sub>2</sub>O<sub>3</sub> catalyst has been used as an industrial catalyst for methanol synthesis from CO<sub>2</sub> hydrogenation. Therefore, Cu-based catalysts have been extensively investigated in CO<sub>2</sub> hydrogenation to methanol and the Cu-ZnO composite is employed as the active species in more than 60% of related reports [25]. However, Cu-based catalysts showed lower selectivity and poor stability because of the competing reverse water-gas shift reaction and the sintering of the active phase, and it was exacerbated by the hydrophilicity of Al<sub>2</sub>O<sub>3</sub>, which could adsorb water generated from the CO<sub>2</sub> hydrogenation. Therefore, there was an urgent need to develop highly efficient catalysts for CO<sub>2</sub> hydrogenation to methanol.

As a typical two-dimensional lamellar material, MoS<sub>2</sub> shows magic physical and chemical properties and is consequently applied in catalysts for hydrogen evolution reactions in electrocatalysis, hydrodesulfurization, and synthesis gas conversions. Early in 1981, Saito and Anderson used MoS<sub>2</sub> as a catalyst for CO<sub>2</sub> hydrogenation at 350 °C, 1 atm, and H<sub>2</sub>/CO<sub>2</sub> = 3.74 [26], while CO was the sole product due to the water gas shift reaction. Combining the electrical conductivity of graphenes with the catalytic activity of MoS<sub>2</sub>, a few layers of MoS<sub>2</sub> platelets supported on few-layers graphene exhibited high catalytic activity for CO<sub>2</sub> hydrogenation, but the major product was methane, frequently with selectivity above 95% and in some cases close to 100% [27]. The catalytic performance of MoS<sub>2</sub> for CO<sub>2</sub> hydrogenation has been studied by density functional theory (DFT) and calculations suggest that MoS<sub>2</sub> could promote the C-O scission of HxCO intermediates, thus explaining the high selectivity of hydrocarbons in the CO<sub>2</sub> hydrogenation process by using molybdenum sulfides as a catalyst [28]. Interestingly, MoS<sub>2</sub> has been used as a support for a single atom in the hydrogenation of CO<sub>2</sub>. The main product was methanol [29]. Zeng et al. have reported that the MoS<sub>2</sub> supporting isolated Pt monomers favored the conversion of CO<sub>2</sub> into methanol, and the selectivity of methanol arrived at 95.4% [30]. These results were thanks to the synergetic interaction between neighboring Pt monomers on MoS<sub>2</sub>. Recently, Wang et al. [31] found that the sulfur vacancy played a key role in the adsorption and activation of CO<sub>2</sub> when the sulfur vacancy-rich MoS<sub>2</sub> was used as a catalyst for the hydrogenation of CO<sub>2</sub>. At 180 °C, the selectivity of methanol was achieved at 94.3% with a 12.5% CO<sub>2</sub> conversion at 3000 mL g<sub>cat.</sub><sup>-1</sup> h<sup>-1</sup> and the catalyst exhibited high stability over 3000 h without any deactivation. However, improving the catalytic performance of molybdenum sulfide in CO<sub>2</sub> hydrogenation to form methanol is still a challenging topic.

Due to anisotropy, the average slab length and layer stacking were important for describing any catalytic active edge sites of MoS<sub>2</sub>. Therefore, adjusting the slab length and layer stacking of MoS<sub>2</sub> would be an effective strategy to generate more active edge sites. Abundant strategies were designed to develop nano-scaled MoS<sub>2</sub> with highly exposed active edge sites to enhance its catalytic activity. In our previous work, MoCS@NSC has been prepared and showed the 97.3% selectivity of MeOH and a 20.0% conversion of CO<sub>2</sub> in the CO<sub>2</sub> hydrogenation [32]. In this catalyst, nano-sized MoS<sub>2</sub> was in-situ generated in the process of preparing nano-sized Mo<sub>2</sub>C confined in carbon material by the pyrolysis of ionic liquid precursors, but its effects on the CO<sub>2</sub> hydrogenation to form methanol were not clear. In the present work, carbon-confining molybdenum sulfide (MoS<sub>2</sub>@C) was designed and prepared using glucose as a carbon source by the in-situ pyrolysis method. On the one side, the carbon layer coating the surface of MoS<sub>2</sub> could improve the adsorption quantity of CO<sub>2</sub>; on the other side, MoS<sub>2</sub> with few layers and little size was prepared by the confinement effect of carbon, which exposed the more active edge sites. As a result, the catalytic performance of MoS<sub>2</sub> in CO<sub>2</sub> hydrogenation to form methanol would be improved. Moreover, the influence of the interaction between MoS<sub>2</sub> and the carbon coating layer on the CO<sub>2</sub> hydrogenation was investigated, and the activation and the conversion route of CO<sub>2</sub> in the presence of MoS<sub>2</sub>@C were also discussed by in situ diffuse reflectance infrared Fourier transform spectroscopy (DRIFTS).

## 2. Experiment

### 2.1. Materials

Glucose, ammonium molybdate, and thiourea (NH<sub>4</sub>)<sub>6</sub>Mo<sub>7</sub>O<sub>24</sub>·4H<sub>2</sub>O, AMT were received from Tianjin Kemiou Chemical Reagent Co., Ltd. (Tianjin, China). CO<sub>2</sub> (99.99%) and 5% Ar/95% H<sub>2</sub> (99.99%) were obtained from Qing Hua Gas Company Limited (Harbin, China), and all reagents were unused and not further purified.

### 2.2. Catalyst Preparation

#### 2.2.1. Synthesis of MoS<sub>2</sub>

The MoS<sub>2</sub> was synthesized according to the literature [31] and as follows: ammonium molybdate (1235.9 mg) and thiourea (2283.6 mg) were dissolved in 20 mL of distilled

water. Then the resulting solution was placed in the glass evaporating dish at 80 °C for 12 h, and the dried mixture was calcined at 550 °C for 2 h in a nitrogen atmosphere, thus generating MoS<sub>2</sub>.

### 2.2.2. Synthesis of MoS<sub>2</sub>@C

Ammonium molybdate (1235.9 mg), thiourea (2283.6 mg), and glucose (9458.4 mg) (the molar ratio of carbon to molybdenum was 45) were dissolved in 35 mL of distilled water. Then the resulting solution was placed in the glass evaporating dish at 80 °C for 12 h, and the dried mixture was calcined at 550 °C for 2 h in a nitrogen atmosphere. Finally, the MoS<sub>2</sub>-45@C was obtained.

According to the same processes, the MoS<sub>2</sub>-5@C sample was prepared when the molar ratio of carbon to molybdenum was reduced to 5 in the precursor.

### 2.2.3. Synthesis of MoS<sub>2</sub>/C

MoS<sub>2</sub>/C catalyst was prepared by the isovolumic impregnation method. Ammonium molybdate (1235.9 mg) and thiourea (2283.6 mg) were dissolved in distilled water. The coconut shell charcoal was added to the solution to achieve a 5% wt. loading. Then the solid was dried at 80 °C and calcined at 550 °C for 2 h under a nitrogen atmosphere. After this process, the MoS<sub>2</sub>/C was prepared.

## 2.3. Catalyst Characterization

The crystalline phase of the catalyst was characterized by X-ray diffraction (XRD) on a D8 Advance with an acceleration voltage of 40 kV.

The microstructure of the catalyst was observed by transmission electron microscopy (TEM) on a JEM-2100 with an acceleration voltage of 200 kV.

The electronic properties of the catalyst surface were determined by X-ray photoelectron spectroscopy (XPS) with an ESCALAB 25, monochromatic Al K $\alpha$ -rays as the X-ray source, and energy of 1486.6 eV.

The CO<sub>2</sub>-programmed temperature desorption (TPD) was performed. A 0.2 g sample was purged at 500 °C for 60 min under He (40 mL/min). It was naturally cooled to 50 °C and adsorbed for 60 min under CO<sub>2</sub> (40 mL/min). The sample was then purged for 30 min in He (40 mL/min) and finally warmed from 50 °C to 400 °C at 10 °C/min in He (40 mL/min) for CO<sub>2</sub> desorption.

In-situ diffuse reflectance and infrared Fourier transform spectroscopy (DRIFTS) measurements were carried out on a Frontier spectrometer by PerkinElmer. The sample was placed directly in the in-situ cell with a ZnSe window and pretreated at 400 °C for 60 min with an H<sub>2</sub> flow of 20 mL/min, and then the background spectrum of the sample was collected from 500 to 4000 cm<sup>-1</sup>. The feed gas H<sub>2</sub>/CO<sub>2</sub> (3/1, 60 mL/min H<sub>2</sub>, 20 mL/min CO<sub>2</sub>) was introduced into the cell. The in-situ DRIFTS were recorded with a resolution of 4 cm<sup>-1</sup> and with an accumulation of 32 scans every 1 min.

## 2.4. Catalytic Performance Test

The activity measurements for CO<sub>2</sub> hydrogenation were performed in a continuous flow high pressure fixed bed reactor (12 mm internal diameter). Prior to the reaction, the catalyst was pretreated in situ for 3 h at 400 °C in pure hydrogen (22 mL/min). After the reactor had cooled to 220 °C, feed gas with an H<sub>2</sub>/CO<sub>2</sub> ratio of 3/1 and a pressure of 3.0 MPa was introduced into the reactor. The effluent was quantified using a Tianmei GC-7900 F and a GC-7890-II gas chromatograph equipped with a flame ionization detector and a thermal conductivity detector, respectively.

## 2.5. Calculation of CO<sub>2</sub> Conversion and Product Selectivity

The CO<sub>2</sub> conversion was calculated by an internal normalization method, and the following Equations (1)–(5) were used for calculating CO<sub>2</sub> conversion and product selectivity.

The CO<sub>2</sub> conversion is expressed as Conv.<sub>CO<sub>2</sub></sub> and the selectivity of the products CO, CH<sub>4</sub>, CH<sub>3</sub>OH and CH<sub>3</sub>OCH<sub>3</sub> is expressed as Sel.<sub>CO</sub>, Sel.<sub>CH<sub>4</sub></sub>, Sel.<sub>CH<sub>3</sub>OH</sub> and Sel.<sub>CH<sub>3</sub>OCH<sub>3</sub></sub> respectively (Equations (1)–(5)). A<sub>CO<sub>2</sub>,out</sub>, A<sub>Ar,in</sub>, A<sub>Ar,out</sub> are the peak areas of the CO<sub>2</sub> and Ar signals at the inlet and tail, in the following order. f<sub>CO<sub>2</sub></sub> and f<sub>Ar</sub> are the correction factors for CO<sub>2</sub> and Ar, in the order of precedence. A<sub>CO,out</sub> and f<sub>CO</sub>, in turn, are the tailpipe signal response area and correction factor for CO. n<sub>CH<sub>4</sub>,out</sub>, n<sub>CH<sub>3</sub>OH,out</sub>, n<sub>CH<sub>3</sub>OCH<sub>3</sub>,out</sub> in order, represent the molarity at the tail gas of CH<sub>4</sub>, CH<sub>3</sub>OH, and CH<sub>3</sub>OCH<sub>3</sub>. n<sub>CO<sub>2</sub>,in</sub> and n<sub>CO<sub>2</sub>,out</sub> are the order of the moles of CO<sub>2</sub> inlet and tail gas.

$$\text{Conv.}_{\text{CO}_2} = \frac{\frac{A_{\text{CO}_2,\text{in}}f_{\text{CO}_2}}{A_{\text{Ar,in}}f_{\text{Ar}}} - \frac{A_{\text{CO}_2,\text{out}}f_{\text{CO}_2}}{A_{\text{Ar,out}}f_{\text{Ar}}}}{\frac{A_{\text{CO}_2,\text{in}}f_{\text{CO}_2}}{A_{\text{Ar,in}}f_{\text{Ar}}}} \times 100\% \quad (1)$$

$$\text{Sel.}_{\text{CO}} = \frac{\frac{A_{\text{CO,out}}f_{\text{CO}}}{A_{\text{Ar,out}}f_{\text{Ar}}}}{\frac{A_{\text{CO}_2,\text{in}}f_{\text{CO}_2}}{A_{\text{Ar,in}}f_{\text{Ar}}} - \frac{A_{\text{CO}_2,\text{out}}f_{\text{CO}_2}}{A_{\text{Ar,out}}f_{\text{Ar}}}} \times 100\% \quad (2)$$

$$\text{Sel.}_{\text{CH}_4} = 100\% \times n_{\text{CH}_4,\text{out}} / (n_{\text{CO}_2,\text{in}} - n_{\text{CO}_2,\text{out}}) \quad (3)$$

$$\text{Sel.}_{\text{CH}_3\text{OH}} = 100\% \times n_{\text{CH}_3\text{OH},\text{out}} / (n_{\text{CO}_2,\text{in}} - n_{\text{CO}_2,\text{out}}) \quad (4)$$

$$\text{Sel.}_{\text{CH}_3\text{OCH}_3} = 100\% \times 2n_{\text{CH}_3\text{OCH}_3,\text{out}} / (n_{\text{CO}_2,\text{in}} - n_{\text{CO}_2,\text{out}}) \quad (5)$$

In addition, the space time yield (STY) of CH<sub>3</sub>OH was calculated according to the following Equation (6):

$$\text{STY} = \frac{FMY}{V_m W} \quad (6)$$

where  $F$  is the volumetric flow rates of CO<sub>2</sub>,  $M$  is the molecular mass of CH<sub>3</sub>OH,  $V_m$  is the molar volume of an ideal gas at standard temperature and pressure (22.414 L/mol),  $W$  is the mass of catalyst, and  $Y$  is the yield of CH<sub>3</sub>OH, respectively.

### 3. Results and Discussions

The crystal phase structure of MoS<sub>2</sub> samples was confirmed by the XRD patterns and is shown in Figure 1. The XRD characteristic diffraction peaks of the bulk MoS<sub>2</sub> were shown at 14.4°, 32.9°, 39.5°, 49.8°, 58.8°, and 69.2°, which were assigned to (002), (100), (103), (105), (110), and (108) crystalline planes of MoS<sub>2</sub> [33]. When MoS<sub>2</sub> was supported on the coconut shell charcoal, except for the characteristic diffraction peak at 2θ of 26° attributed to graphitic carbon [34], there was also a weaker diffraction peak at 2θ of 44.2°, which was assigned to the (105) crystallographic plane of MoS<sub>2</sub>. It was suggested that MoS<sub>2</sub> was successfully supported on coconut shell charcoal. When the molar ratio of carbon to molybdenum is 45 in the precursor, the resulting MoS<sub>2</sub>-45@C only shows a broad diffraction peak at 2θ of 26°, which corresponds to the (002) planar diffraction peak of graphite [34]. While the characteristic diffraction peaks of MoS<sub>2</sub> were not apparent, it was due to the high dispersion of MoS<sub>2</sub>.

When the molar ratio of carbon to molybdenum was decreased to 5 in the precursor, the characteristic diffraction peaks of MoS<sub>2</sub>-5@C shown at 32.9°, 39.5°, and 58.8° were attributed to the (100), (103), and (110) crystallographic planes of MoS<sub>2</sub>, respectively. These results confirmed that the carbon, which was formed by in-situ pyrolysis, showed the confinement effect on the synthesis of MoS<sub>2</sub>.

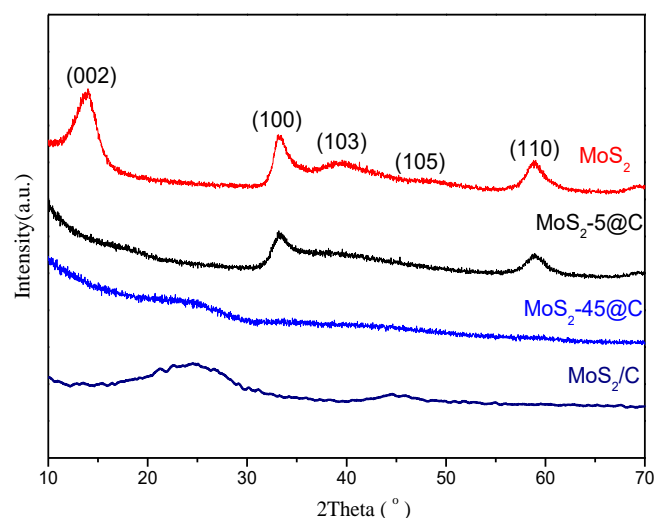


**Figure 1.** XRD patterns of MoS<sub>2</sub> samples.

It also can be seen that all patterns are characterized by broad reflections with low intensities, and these observations are clear hints for the poor crystallinity and sizes of coherent scattering domains within the nano regime. Compared with the bulk MoS<sub>2</sub> sample, the intensity of the (002) reflection at  $2\theta$  of 14° disappeared for the samples MoS<sub>2</sub>/C, MoS<sub>2</sub>-5@C, and MoS<sub>2</sub>-45@C. This observation can be explained by the decreasing number of stacked MoS<sub>2</sub> slabs in the products [35]. These results also indicated the confinement effects of in-situ formation carbon could suppress the growth of MoS<sub>2</sub> grains.

To further enlighten the structure of MoS<sub>2</sub>, transmission electron microscopy (TEM) and high-resolution TEM (HRTEM) analyses were also carried out. From Figure 2a, it can be seen that the bulk MoS<sub>2</sub> has more layers on the edge, and the thicker part in the middle is not even visible. The clear lattice striations on the surface clearly show that the crystal plane spacing is 0.62 nm, corresponding to the (002) crystal plane of MoS<sub>2</sub>. Compared with bulk MoS<sub>2</sub>, MoS<sub>2</sub>/C is limited by the pores of the coconut shell charcoal (Figure 2b), and the layer number of MoS<sub>2</sub> in MoS<sub>2</sub>/C was decreased to 7, which corresponded to the results of XRD. These results suggested that loaded on the support was beneficial to reduce the layers of MoS<sub>2</sub> [36–38]. The image of Figure 2c showed MoS<sub>2</sub> with fewer layers and the smaller practical was obtained successfully in MoS<sub>2</sub>-45@C when the carbon was in situ formed from the pyrolysis of glucose, and it was beneficial to expose the more active site at the edges for the CO<sub>2</sub> hydrogenation. The SAED patterns (Figure 2d) demonstrate the low crystallinity of MoS<sub>2</sub>, which matches the XRD results.

An X-ray photoelectron spectroscopy (XPS) characterization was carried out to further study the element chemical states in MoS<sub>2</sub> samples. Figure S1 and Table S1 showed the XPS survey spectra of the samples under study, and the numerical values of the surface composition obtained from these spectra were given in Table S1. The elements of Mo, S, C, and O were detected on the surface of all samples, and the N element was also found on the surface of MoS<sub>2</sub>/C and MoS<sub>2</sub>-45@C. Note that the ratio of the Mo and S in bulk MoS<sub>2</sub> followed the chemical formula, while the ratio of the Mo and S in MoS<sub>2</sub>/C and MoS<sub>2</sub>-45@C was lower than the chemical formula. These results indicate that the carbon material was doped by the S element when the MoS<sub>2</sub> was generated in MoS<sub>2</sub>/C and MoS<sub>2</sub>-45@C.

Figure 3a and Table S2 show the high-resolution XPS spectrum in the Mo 3d region, and the Mo 3d peaks of the bulk MoS<sub>2</sub> sample with binding energies of 232.0 and 229.1 eV are indexed to Mo 3d<sub>3/2</sub> and Mo 3d<sub>5/2</sub>, respectively, indicating the presence of Mo<sup>4+</sup> of molybdenum disulfide [39]. In addition, a small peak at 226.1 eV was found and assigned to S 2s [39]. In XPS of MoS<sub>2</sub>/C, there are two prominent peaks assigned to Mo 3d<sub>3/2</sub> and Mo 3d<sub>5/2</sub> (232.0 eV and 229.1 eV), which demonstrate the existence of Mo<sup>4+</sup> and the successful synthesis of MoS<sub>2</sub> [40]. Additionally, the peaks at 232.8 and 235.9 eV can be ascribed to Mo<sup>6+</sup> 3d<sub>5/2</sub> and 3d<sub>3/2</sub>, which were formed by the surface oxidation of MoS<sub>2</sub> [41–43].

Compared with MoS<sub>2</sub>/C, the characteristic peaks corresponding to Mo<sup>4+</sup> and Mo<sup>6+</sup> were also found, but the binding energy between the Mo<sup>6+</sup> 3d<sub>5/2</sub> and 3d<sub>3/2</sub> in MoS<sub>2</sub>-45@C gave a negative shift (0.4 eV), suggesting that the electron interactions between carbon and the MoS<sub>2</sub> surface in MoS<sub>2</sub>-45@C were stronger than in MoS<sub>2</sub>/C. It is worth mentioning that the two obvious peaks centered at 231.1 and 228.0 eV imply the existence of a C-Mo bond, further confirming the stronger interfacial interaction between the MoS<sub>2</sub> surface and the carbon coating layer in MoS<sub>2</sub>-45@C [44], which could weaken the Mo-S bond [45].

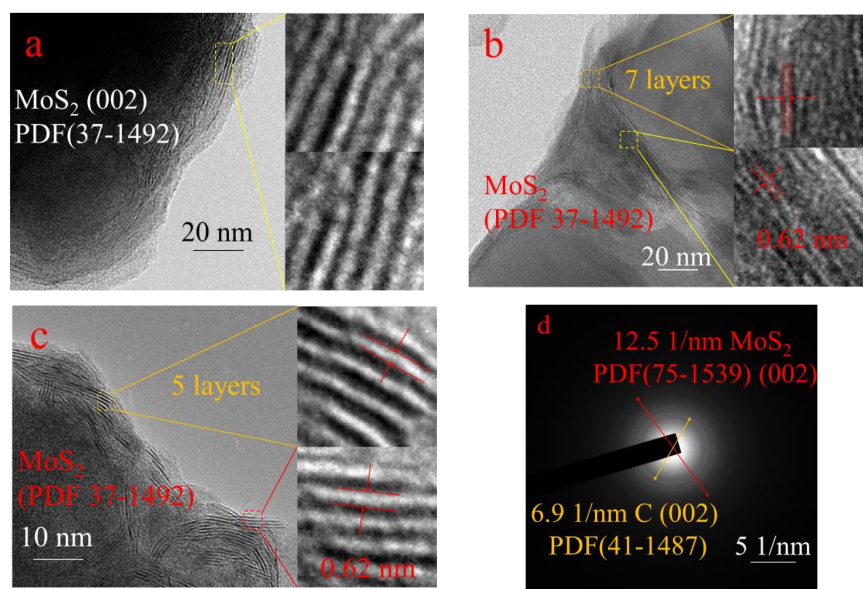


**Figure 2.** Catalyst characterization: (a) MoS<sub>2</sub> TEM (20 nm); (b) MoS<sub>2</sub>/C TEM (20 nm); (c) MoS<sub>2</sub>-45@C HRTEM (10 nm); (d) MoS<sub>2</sub>-45@C SAED (5 1/nm).

As exhibited in Figure 3b and Table S3, the S 2p spectra of the bulk MoS<sub>2</sub> sample showed two strong peaks at 163.2 eV and 161.8 eV for the S2p<sub>1/2</sub> and S2p<sub>3/2</sub> binding energies of S<sup>2-</sup> [46,47]. The electron binding energy of S 2p<sub>3/2</sub> of S<sup>2-</sup> in MoS<sub>2</sub>/C and MoS<sub>2</sub>-45@C had a negative shift of about 0.3 eV compared with MoS<sub>2</sub>, respectively. It indicated the existence of electron interactions between the carbon coating layer and the MoS<sub>2</sub> surface. Moreover, the doublet peaks at 163.7 and 164.8 eV were found, and they were assigned to S<sub>2</sub><sup>2-</sup> and apical S<sup>2-</sup>, which indicates the formation of sulfur vacancies on the catalyst surface [48]. The sulfur vacancies could induce the charge-density redistribution, thus producing much more active sites on the catalyst surface. Except, so far, the peak with a binding energy of 168.3 eV was detected in the XPS of MoS<sub>2</sub>/C and MoS<sub>2</sub>-45@C, which resulted from the surface oxidation of sulfur elements, and it was contributed to the presence of a sulfate group [49].

In addition, three peaks were present at 395.1 eV, 398.2–398.6 eV, and 400.1–400.5 eV in the N1s high-resolution XPS spectrum of MoS<sub>2</sub>-45@C and MoS<sub>2</sub>/C (Figure S2 and Table S4), which can be assigned to Mo3p, pyridinic-N, and pyrrolic-N [49]. It was mentioned that the binding energy of pyridinic-N and pyrrolic-N in MoS<sub>2</sub>-45@C was 0.4 eV lower than that in MoS<sub>2</sub>/C, demonstrating an increased electron cloud density around nitrogen in MoS<sub>2</sub>-45@C, which was benefited by the adsorption of CO<sub>2</sub> on its surface.

Moreover, observing the C 1s spectra of MoS<sub>2</sub>-45@C, it was clearly divided into five fitted peaks at 284.5, 285.2, 286.1, 286.6, and 288.6 eV, which can be related to C-C, C-O, C-O-C/S, C-O-Mo, and C=O (Figure S3 and Table S5). It shows that MoS<sub>2</sub> could also be tightly linked with carbon by the C-O-Mo bond, being conducive to the MoS<sub>2</sub> confined in the carbon coating layer [44]. As shown in Figure S4 and Table S6, the peaks in the O1s spectrum at 533.3 eV, 532.5 eV, 531.7 eV, and 530.8 eV are for the Mo-O, C-OH, C-O/O-C-N, and O=C groups, respectively [50].

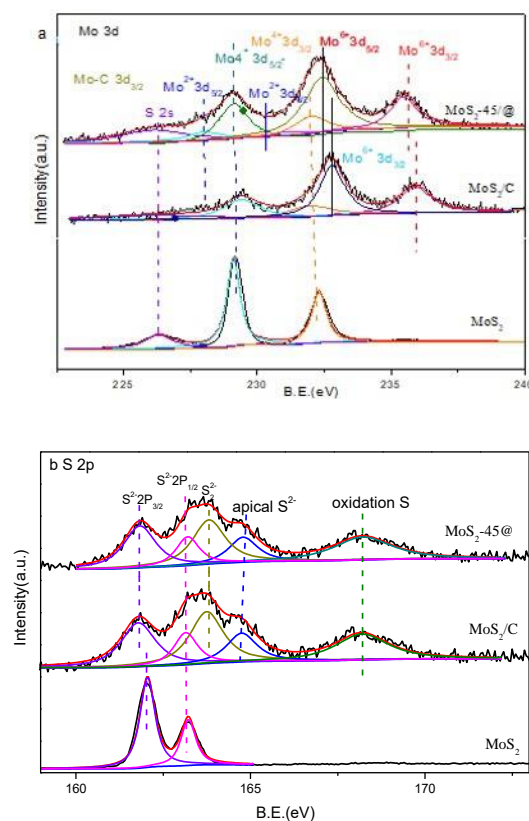


**Figure 3.** XPS of different catalyst: (a) Mo3d and (b) S2p.

Due to the dual-site mechanism for CO<sub>2</sub> hydrogenation, the adsorption and the activation of CO<sub>2</sub> occur on the surface of the supporter, implying that the activity and conversion of CO<sub>2</sub> are closely related to the surface basicity of the supporter [25,51–54]. The CO<sub>2</sub>-TPD experiments were carried out, and the results are shown in Figure 4 and Figure S5. The temperature of the CO<sub>2</sub> desorption peak was increased with the order bulk MoS<sub>2</sub> < MoS<sub>2</sub>/C < MoS<sub>2</sub>@C < NSC (N,S-codoping carbon), and the area of the CO<sub>2</sub> desorption peak was also raised in the same order, suggesting the basic strength and the number of basic sites were enhanced with the order bulk MoS<sub>2</sub> < MoS<sub>2</sub>/C < MoS<sub>2</sub>@C < NSC. It was due to the strong acid-base interactions between the basic S-C functional group and the acidic CO<sub>2</sub> molecule in the carbon skeleton and the strong dipole-dipole interaction between the large quadrupole moment of the CO<sub>2</sub> molecule and the polar sites associated with the sulfur functional group [55].

Under 220 °C, 3 MPa, and a gas hourly space velocity (GHSV) of 5670 mL h<sup>-1</sup> g<sub>cat.</sub><sup>-1</sup>, the catalytic performance was evaluated in a fixed-bed reactor, and the results are listed in Table 1. As a reference catalyst, the catalytic performance of NSC was investigated first, and the result showed CO<sub>2</sub> could not be converted, suggesting that NSC had no catalytic activity in the CO<sub>2</sub> hydrogenation, although it exhibited the highest CO<sub>2</sub> adsorption capacity. Employing MoS<sub>2</sub> as a catalyst, the selectivity of methanol arrived at 66.9% with the 18.3% conversion of CO<sub>2</sub>, and methane, as the major byproduct, was found with a 32.7% selectivity. Meanwhile, dimethyl ether (DME) was also detected with a 0.4% selectivity. These results indicated that MoS<sub>2</sub> displayed catalytic activity for CO<sub>2</sub> hydrogenation, but the selectivity of methanol was lower, and the high selectivity of methane was given. Using MoS<sub>2</sub>-45@C as an alternative catalyst, the selectivity of methanol was improved to 95.8% with the 27.3% conversion of CO<sub>2</sub>, the selectivity of methane was reduced to 4.2%, and DME was not detected. Additionally, the STY of methanol arrived at 0.538 gg<sub>cat.</sub><sup>-1</sup> h<sup>-1</sup> in the presence of MoS<sub>2</sub>-45@C. On the one hand, exposing the more active sites to thin and small MoS<sub>2</sub> and the higher carbon dioxide adsorption capacity of MoS<sub>2</sub>-45@C were beneficial for accelerating the CO<sub>2</sub> conversion due to the dual-site mechanism for CO<sub>2</sub>

hydrogenation, and the complete decomposition of CO<sub>2</sub> on the surface of MoS<sub>2</sub>-45@C was inhibited by the higher carbon dioxide adsorption capacity, which was conducive to improving methanol selectivity [56–58]. On the other hand, the stronger interaction of MoS<sub>2</sub> and the carbon coating layer in MoS<sub>2</sub>-45@C was also beneficial to CO<sub>2</sub> hydrogenation by decreasing the Gibbs free energy of hydrogen adsorption [43]. Moreover, the high selectivity of methanol was also thanks to the additional S-vacancy in the MoS<sub>2</sub>-45@C catalyst (Figure S6) [31]. When the molar ratio of carbon to molybdenum was decreased to 5 in the precursor, the MoS<sub>2</sub>-5@C gave a 79.9% selectivity of methanol with an 18.4% conversion of CO<sub>2</sub>. These results were probably because the larger size of MoS<sub>2</sub> and the less active site were exposed. The compared catalyst, MoS<sub>2</sub>/C, showed a 78.5% selectivity of methanol, while the conversion was very low (only 4.2%). This was due to the fact that the 5% loading capacity of MoS<sub>2</sub> on the coconut shell carbon was too low, which resulted in a large amount of adsorbed CO<sub>2</sub> that could not be efficiently converted.

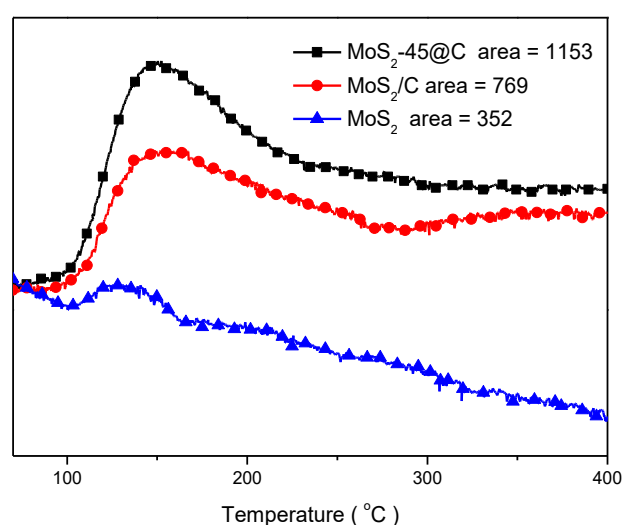


**Figure 4.** CO<sub>2</sub>-TPD curves of MoS<sub>2</sub>-45@C, MoS<sub>2</sub>/C and MoS<sub>2</sub>.

**Table 1.** The performance of catalyst in CO<sub>2</sub> hydrogenation [a].

Catalyst	Conversion/%	Selectivity/%			STY /g <sub>MeOH</sub> g <sub>cat.</sub> <sup>-1</sup> h <sup>-1</sup>
		CH <sub>3</sub> OH	CH <sub>4</sub>	CH <sub>3</sub> OCH <sub>3</sub>	
NSC	-	-	-	-	-
MoS <sub>2</sub>	18.3	66.9	32.7	0.4	0.252
MoS <sub>2</sub> -45@C	27.3	95.8	4.2	0	0.538
MoS <sub>2</sub> -5@C	18.4	79.9	20.1	0	0.302
MoS <sub>2</sub> /C	4.2	78.5	21.5	0	0.068

[a] Reaction conditions: 160 °C, 3 MPa, GHSV 5670 mL g<sub>cat.</sub><sup>-1</sup> h<sup>-1</sup>, V<sub>H<sub>2</sub></sub>/V<sub>CO<sub>2</sub></sub> = 3.

In the presence of MoS<sub>2</sub>-45@C, the reaction conditions were optimized, and the results are shown in Figure 5. Firstly, the effects of reaction temperature on the catalytic performance were investigated (Figure 5a).

It can be seen that the CO<sub>2</sub> conversion was increased by enhancing the reaction temperature, and it was improved from 26.3% to 32.6% by raising the temperature from 140 °C to 240 °C. These results indicated that MoS<sub>2</sub>-45@C exhibited higher catalytic activity at a low temperature. When the reaction was performed at 140 °C, 89.0% selectivity of methanol was given, and the methane selectivity reached 11.0%. With increasing reaction temperature to 160 °C, the selectivity of methanol was improved to 95.8%. Further raising the reaction temperature to 240 °C, the selectivity of methanol was reduced, and an 82.6% selectivity of methanol was obtained. It was probably because the too high reaction temperature contributed to the full decomposition of CO<sub>2</sub> on the catalyst surface and

enhanced the catalytic hydrogenation activity, which contributed to the high selectivity of methane. Additively, CO was found when the reaction was performed at 240 °C in the presence of MoS<sub>2</sub>-45@C.

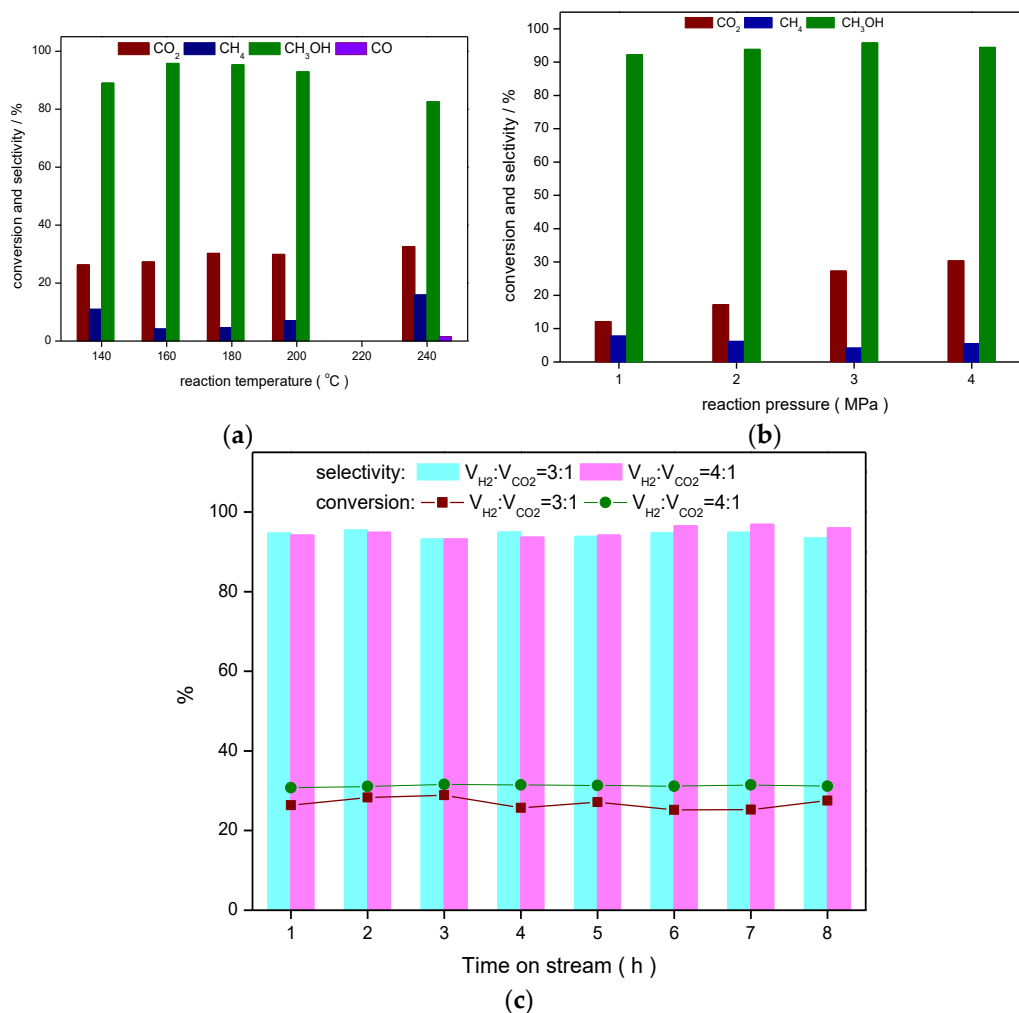


**Figure 5.** Optimized reaction conditions: (a) reaction temperatures, (b) reaction pressures, (c) ratio of H<sub>2</sub> to CO<sub>2</sub>.

Controlling the reaction temperature at 160 °C, the effects of pressure on the CO<sub>2</sub> hydrogenation were evaluated by using MoS<sub>2</sub>-45@C as a catalyst (Figure 5b). With increasing the reaction pressure, the CO<sub>2</sub> conversion was gradually increased with no significant change in methanol selectivity. These results suggest the higher reaction pressure has a positive effect on the CO<sub>2</sub> conversion. It was because the CO<sub>2</sub> hydrogenation was a volume reduction reaction. At the same time, the higher reaction pressure was advantageous for the adsorption of CO<sub>2</sub> on the surface of MoS<sub>2</sub>-45@C, which was favorable for the conversion of CO<sub>2</sub>. In Figure 5b, it is worth noting that the 12.2% conversion of CO<sub>2</sub> and the 92.2% selectivity of methanol were given when the reaction pressure was reduced to 1 MPa. These results suggested that MoS<sub>2</sub>-45@C displayed a highly catalytic performance under the low reaction pressure. Following that, the influence of the ratio of H<sub>2</sub> and CO<sub>2</sub> in the feed gas on the CO<sub>2</sub> hydrogenation was also investigated (Figure 5c). The results showed the CO<sub>2</sub> conversion was susceptible to the ratio of H<sub>2</sub> and CO<sub>2</sub> in the feed gas, while the selectivity of methanol was kept almost unchanged.

Stability is a fatal issue for the catalysts, which were used in CO<sub>2</sub> hydrogenation. Under the optimal reaction conditions, the stability of MoS<sub>2</sub>-45@C was investigated in a fixed-bed reactor, and the results are shown in Figure 6. In the first 20 h, the CO<sub>2</sub> conversion,

the methanol selectivity, and STY were increased with prolonged reaction time, while the methane selectivity was decreased. When the reaction time was more than 20 h, the catalytic performance of MoCS-45@C was kept stable. The CO<sub>2</sub> conversion was stabilized at around 32.4%, with about 94.8% selectivity of methanol. During the reaction period of 150 h, the catalytic performance of MoCS-45@C showed almost no attenuation, which suggests a promising prospect for industrial applications.

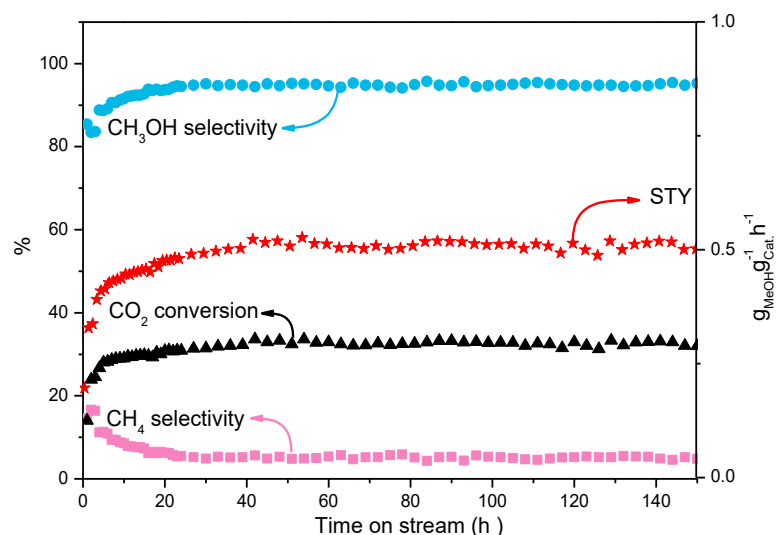


**Figure 6.** Stability of the MoS<sub>2</sub>-45@C catalyst with granule stacking.

To propose a reaction sequence and a surface reaction mechanism, in situ diffuse reflectance infrared Fourier transform spectroscopy (in situ DRIFTS) was used to identify the evolution of surface species on the surface of MoS<sub>2</sub>-45@C. The in-situ drift spectra for the hydrogenation of CO<sub>2</sub> to methanol over MoS<sub>2</sub>-45@C at 180 °C with time were shown in Figure 7, and detailed information on the evolution of intermediate species could be found.

Firstly, the pure CO<sub>2</sub> was introduced into the MoS<sub>2</sub>-45@C catalyst (Figure 7a), and the IR bands at 1420, 1437, 1458, 1522, 1542, and 1575 cm<sup>-1</sup> were observed, which were assigned to adsorbed \*CO<sub>2</sub> species [59–63]. Moreover, IR bands at 1474 and 1558 cm<sup>-1</sup> also came into the formation, assigned to bidentate carbonate [59,64], and the signals of monodentate carbonate species were prevalent at 1490 and 1508 cm<sup>-1</sup> [64,65]. Additionally, their intensities were increased by prolonging the contact time of CO<sub>2</sub> and MoS<sub>2</sub>-45@C from 1 min to 8 min. These results indicated that CO<sub>2</sub> could be adsorbed on the surface of the MoS<sub>2</sub>-45@C catalyst, and the adsorption capacity of CO<sub>2</sub> was improved by prolonging the contact time of CO<sub>2</sub> and MoS<sub>2</sub>-45@C. It was worth noting that the IR bands at 2078 and 2094 cm<sup>-1</sup> were found when the MoS<sub>2</sub>-45@C catalyst was exposed to the CO<sub>2</sub> atmosphere. These results indicated that CO<sub>2</sub> was dissociated to yield surface-bound CO\* on the catalytic surface [56,58,66], and their intensities were increased as time went on. These results would be beneficial for increasing the selective synthesis of methanol from the CO<sub>2</sub> hydrogenation [31]. Then, the feeding gas was switched from pure CO<sub>2</sub> to H<sub>2</sub> (Figure 7b), and the CO\* peaks from the dissociation of CO<sub>2</sub> gradually disappeared with the rise of CH<sub>3</sub>O\* peaks (2864 and 2917 cm<sup>-1</sup>) [62,67], and the intensity of which decreased as time went on, thereby indicating the hydrogenation of CO\* to CH<sub>3</sub>O\* and then the formation of CH<sub>3</sub>OH. At the same time, a weak shoulder peak that appeared at 2957 cm<sup>-1</sup> in the ν (CH) region was also detected, and it was a combination of the CH bending and asymmetric OCO stretching modes of formate species (HCOO\*) [60,68]. It was indicated the carbonate species adsorbed on the surface of the MoS<sub>2</sub>-45@C catalyst were also hydrogenated. These results explain the decrease in the peaks intensity of the carbonate species when H<sub>2</sub> was introduced. Moreover, the IR bonds at 2850 cm<sup>-1</sup> were also found, and they were assigned to the symmetric and asymmetric H<sub>2</sub>CO\* stretching vibrations [60,69], respectively, which

might derive from both formate and CO-hydro pathways. These results confirmed that both CO and formate were significant intermediate species for CO<sub>2</sub> hydrogenation to methanol over the MoS<sub>2</sub>-45@C catalyst. Exposing MoS<sub>2</sub>-45@C to the feed gas (CO<sub>2</sub> + H<sub>2</sub>), similar in-situ drift IR spectra were obtained (Figure 3c), and these results suggested that the HCOO\* hydrogenation route and the CO\* hydrogenation route were performed simultaneously in the presence of the MoS<sub>2</sub>-45@C catalyst in the CO<sub>2</sub> hydrogenation. Hence, combining the results of in-situ DRIFTS with the literature [56–69], we held the opinion that the hydrogenation of HCOO\* and CO\* were all carried out when MoS<sub>2</sub>-45@C was employed as a catalyst in the CO<sub>2</sub> hydrogenation (Figure 8).

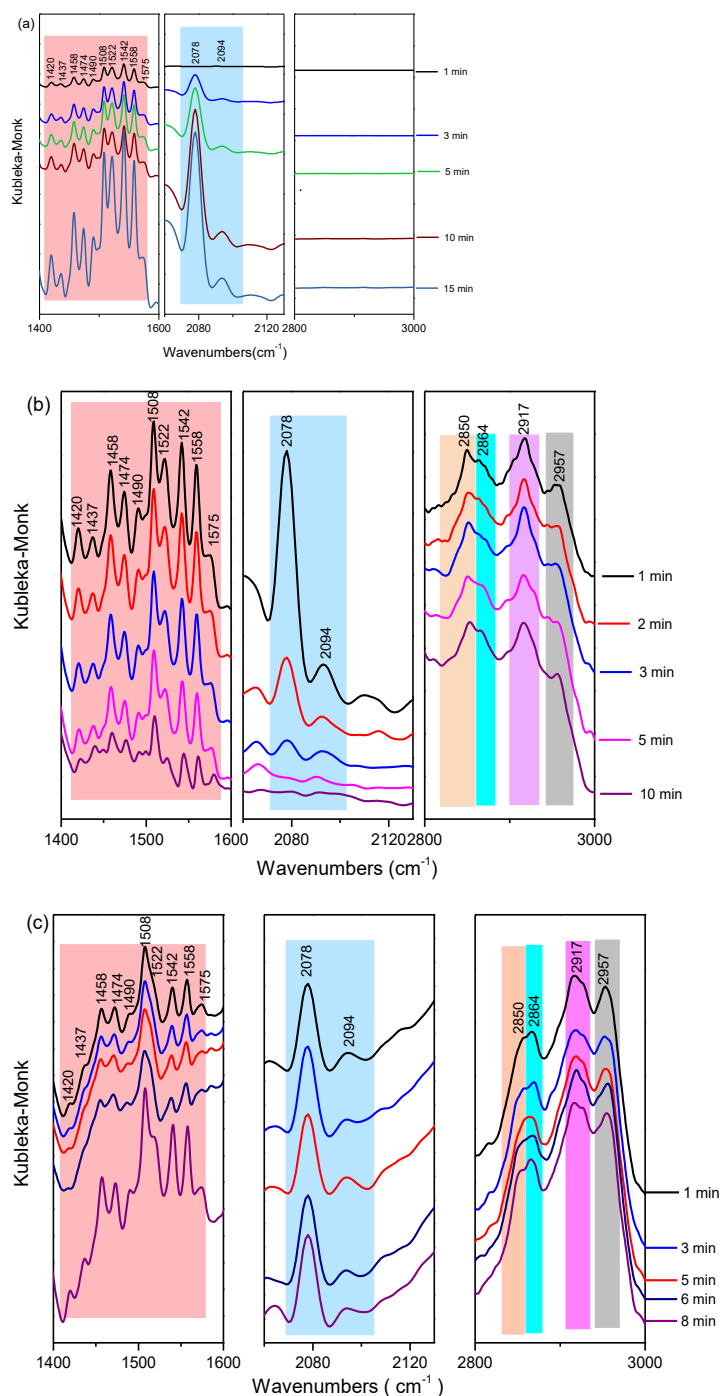


**Figure 7.** In situ DRIFTS spectra of CO<sub>2</sub> hydrogenation on MoS<sub>2</sub>-45@C: different feed introduced to catalyst (a) CO<sub>2</sub>; (b) H<sub>2</sub>; (c) CO<sub>2</sub> + H<sub>2</sub>.

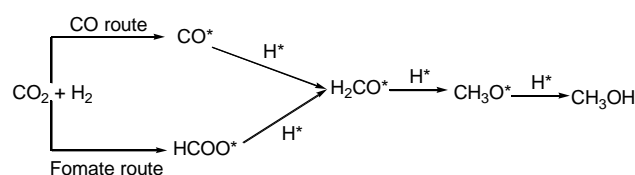


**Figure 8.** Reaction route for CO<sub>2</sub> hydrogenation to methanol over MoS<sub>2</sub>-45@C.

#### 4. Conclusions

In conclusion, comparing MoS<sub>2</sub>/C and bulk MoS<sub>2</sub> samples, carbon-confining MoS<sub>2</sub> in MoS<sub>2</sub>-45@C samples prepared by the in-situ pyrolysis method had the characteristics of few layers and small size, which were beneficial to exposing the more active sites. The strong interaction between MoS<sub>2</sub> and the carbon coating layer in the MoS<sub>2</sub>-45@C catalyst was formed, which was also favorable to the CO<sub>2</sub> hydrogenation by decreasing the Gibbs free energy of hydrogen adsorption. Moreover, the adsorption capacity of CO<sub>2</sub> on the MoS<sub>2</sub>-45@C surface was improved when the carbon coating layer was doped with sulfur and nitrogen, which also contributed to the CO<sub>2</sub> conversion and the methanol selectivity. Under the optimal reaction conditions, the MoS<sub>2</sub>-45@C showed excellent catalytic performance and catalytic stability, and there was no deactivation in CO<sub>2</sub> hydrogenation for more than 150 h on stream at least, which indicates a promising potential for industrial applications.

**Supplementary Materials:** The following supporting information can be downloaded at: <https://www.mdpi.com/article/10.3390/ijms23095220/s1> [70–74].

**Author Contributions:** P.C.: Investigation, Formal analysis, Writing—original draft. R.S.: characterization. L.X.: Conceptualization, Methodology, Writing—review and editing. W.W.: Visualization, Writing—review and editing, Supervision, Project administration. All authors have read and agreed to the published version of the manuscript.

**Funding:** This research was funded by the financial supports from the National Key Research and Development Project, Intergovernmental International Science and Technology Innovation Cooperation Key Project (2018YFE0108800).

**Institutional Review Board Statement:** Not applicable.

**Informed Consent Statement:** Not applicable.

**Data Availability Statement:** Not applicable.

**Acknowledgments:** The authors acknowledge the financial supports from the National Key Research and Development Project, Intergovernmental International Science and Technology Innovation Cooperation Key Project (2018YFE0108800).

**Conflicts of Interest:** The authors declare no conflict of interest.

#### References

- Wei, J.; Yao, R.; Han, Y.; Ge, Q.; Sun, J. Towards the development of the emerging process of CO<sub>2</sub> heterogeneous hydrogenation into high-value unsaturated heavy hydrocarbons. *Chem. Soc. Rev.* **2021**, *50*, 10764–10805. [[CrossRef](#)] [[PubMed](#)]
- Jiang, X.; Nie, X.; Guo, X.; Song, C.; Chen, J.G. Recent advances in carbon dioxide hydrogenation to methanol via heterogeneous catalysis. *Chem. Rev.* **2020**, *120*, 7984–8034. [[CrossRef](#)] [[PubMed](#)]
- Xu, D.; Wang, Y.Q.; Ding, M.Y.; Hong, X.L.; Liu, G.L.; Tsang, S.C.E. Advances in higher alcohol synthesis from CO<sub>2</sub> hydrogenation. *Chem* **2021**, *7*, 849–881. [[CrossRef](#)]
- Bediako, B.B.A.; Qian, Q.; Han, B.X. Synthesis of C<sub>2+</sub> Chemicals from CO<sub>2</sub> and H<sub>2</sub> via C-C Bond Formation. *Acc. Chem. Res.* **2021**, *54*, 2467–2476. [[CrossRef](#)] [[PubMed](#)]
- Sancho-Sanz, I.; Korili, S.A.; Gil, A. Catalytic valorization of CO<sub>2</sub> by hydrogenation: Current status and future trends. *Catal. Rev.* **2021**. [[CrossRef](#)]
- Wang, D.; Xie, Z.H.; Porosoff, M.D.; Chen, J.G. Recent advances in carbon dioxide hydrogenation to produce olefins and aromatics. *Chem* **2021**, *7*, 2277–2311. [[CrossRef](#)]
- Navarro-Jaén, S.; Virginie, M.; Bonin, J.; Robert, M.; Wojcieszak, R.; Khodakov, A.Y. Highlights and challenges in the selective reduction of carbon dioxide to methanol. *Nat. Rev. Chem.* **2021**, *5*, 564–579. [[CrossRef](#)]

8. Bai, S.T.; De Smet, G.; Liao, Y.H.; Sun, R.Y.; Zhou, C.; Beller, M.; Maes, B.U.W.; Sels, B.F. Homogeneous and heterogeneous catalysts for hydrogenation of CO<sub>2</sub> to methanol under mild conditions. *Chem. Soc. Rev.* **2021**, *50*, 4259–4298. [[CrossRef](#)]
9. Zhang, X.B.; Zhang, G.H.; Song, C.S.; Guo, X.W. Catalytic conversion of carbon dioxide to methanol: Current status and future perspective. *Front. Energy Res.* **2021**, *8*, 621119. [[CrossRef](#)]
10. Sharma, P.; Sebastian, J.; Ghosh, S.; Creaser, D.; Olsson, L. Recent advances in hydrogenation of CO<sub>2</sub> into hydrocarbons via methanol intermediate over heterogeneous catalysts. *Catal. Sci. Technol.* **2021**, *11*, 1665–1697. [[CrossRef](#)]
11. Murthy, P.S.; Liang, W.B.; Jiang, Y.J.; Huang, J. Cu-Based Nanocatalysts for CO<sub>2</sub> hydrogenation to methanol. *Energy Fuels* **2021**, *35*, 8558–8584. [[CrossRef](#)]
12. Shi, Z.; Tan, Q.; Wu, D. Enhanced CO<sub>2</sub> hydrogenation to methanol over TiO<sub>2</sub> nanotubes-supported CuO-ZnO-CeO<sub>2</sub> catalyst. *Appl. Catal. A Gen.* **2019**, *581*, 58–66. [[CrossRef](#)]
13. Zhang, G.; Fan, G.; Yang, L.; Li, F. Tuning surface-interface structures of ZrO<sub>2</sub> supported copper catalysts by in situ introduction of indium to promote CO<sub>2</sub> hydrogenation to methanol. *Appl. Catal. A Gen.* **2020**, *605*, 117805. [[CrossRef](#)]
14. Snider, J.L.; Streibel, V.; Hubert, M.A.; Choksi, T.S.; Valle, E.; Upham, D.C.; Schumann, J.; Duyar, M.S.; Gallo, A.; Abild-Pedersen, F.; et al. Revealing the synergy between oxide and alloy phases on the performance of bimetallic In-Pd catalysts for CO<sub>2</sub> hydrogenation to methanol. *ACS Catal.* **2019**, *9*, 3399–3412. [[CrossRef](#)]
15. Gholinejad, M.; Khosravi, F.; Afrasi, M.; Sansano, J.M.; Nájera, C. Applications of bimetallic PdCu catalysts. *Catal. Sci. Technol.* **2021**, *11*, 2652–2702. [[CrossRef](#)]
16. Sha, F.; Han, Z.; Tang, S.; Wang, J.; Li, C. Hydrogenation of carbon dioxide to methanol over non-Cu-based heterogeneous catalysts. *ChemSusChem* **2020**, *13*, 6160–6181. [[CrossRef](#)] [[PubMed](#)]
17. Khobragade, R.; Roškarič, M.; Žerjav, G.; Košiček, M.; Zavašnik, J.; Van de Velde, N.; Jerman, I.; Tušar, N.N.; Pintar, A. Exploring the effect of morphology and surface properties of nanoshaped Pd/CeO<sub>2</sub> catalysts on CO<sub>2</sub> hydrogenation to methanol. *Appl. Catal. A Gen.* **2021**, *667*, 118394. [[CrossRef](#)]
18. Lin, F.; Jiang, X.; Boreriboon, N.; Wang, Z.; Song, C.; Cen, K. Effects of supports on bimetallic Pd-Cu catalysts for CO<sub>2</sub> hydrogenation to methanol. *Appl. Catal. A Gen.* **2019**, *585*, 117210. [[CrossRef](#)]
19. Nie, X.W.; Li, W.H.; Jiang, X.; Guo, X.W.; Song, C.S. Recent advances in catalytic CO<sub>2</sub> hydrogenation to alcohols and hydrocarbons. *Adv. Catal.* **2020**, *65*, 121–233.
20. Shen, C.Y.; Bao, Q.Q.; Xue, W.J.; Sun, K.H.; Zhang, Z.T.; Jia, X.Y.; Mei, D.H.; Liu, C.J. Synergistic effect of the metal-support interaction and interfacial oxygen vacancy for CO<sub>2</sub> hydrogenation to methanol over Ni/In<sub>2</sub>O<sub>3</sub> catalyst: A theoretical study. *J. Energy Chem.* **2022**, *65*, 623–629. [[CrossRef](#)]
21. Wang, J.Y.; Zhang, G.H.; Zhu, J.; Zhang, X.B.; Ding, F.S.; Zhang, A.F.; Guo, X.W.; Song, C.S. CO<sub>2</sub> hydrogenation to methanol over In<sub>2</sub>O<sub>3</sub>-based catalysts: From mechanism to catalyst development. *ACS Catal.* **2021**, *11*, 1406–1423. [[CrossRef](#)]
22. Wang, J.J.; Tang, C.Z.; Li, G.N.; Han, Z.; Li, Z.L.; Liu, H.; Cheng, F.; Li, C. High-performance MaZrO<sub>x</sub> (Ma = Cd, Ga) solid-solution catalysts for CO<sub>2</sub> hydrogenation to methanol. *ACS Catal.* **2019**, *9*, 10253–10259. [[CrossRef](#)]
23. Wang, J.J.; Li, G.N.; Li, Z.L.; Tang, C.Z.; Feng, Z.C.; An, H.Y.; Liu, H.L.; Liu, T.F.; Li, C. A highly selective and stable ZnO-ZrO<sub>2</sub> solid solution catalyst for CO<sub>2</sub> hydrogenation to methanol. *Sci. Adv.* **2017**, *3*, e1701290. [[CrossRef](#)] [[PubMed](#)]
24. Xu, D.; Hong, X.L.; Liu, G.L. Highly dispersed metal doping to ZnZr oxide catalyst for CO<sub>2</sub> hydrogenation to methanol: Insight into hydrogen spillover. *J. Catal.* **2021**, *393*, 207–214. [[CrossRef](#)]
25. Qiao, S.C.; Liu, X.Y.; Zhu, R.R.; Xue, D.M.; Liu, X.Q.; Sun, L.B. Causation of catalytic activity of Cu-ZnO for CO<sub>2</sub> hydrogenation to methanol. *Chem. Eng. J.* **2022**, *430*, 132784. [[CrossRef](#)]
26. Saito, M.; Anderson, R.B. The activity of several molybdenum compounds for the methanation of CO<sub>2</sub>. *J. Catal.* **1981**, *67*, 296–302. [[CrossRef](#)]
27. Primo, A.; He, J.; Jurca, B.; Cojocaru, B.; Bucur, C.; Parvulescu, V.I.; Garcia, H. CO<sub>2</sub> methanation catalyzed by oriented MoS<sub>2</sub> nanoplatelets supported on few layers graphene. *Appl. Catal. B Environ.* **2019**, *245*, 351–359. [[CrossRef](#)]
28. Liu, P.; Choi, Y.M.; Yang, Y.; White, M.G. Methanol synthesis from H<sub>2</sub> and CO<sub>2</sub> on a Mo<sub>6</sub>S<sub>8</sub> cluster: A density functional study. *J. Phys. Chem. A* **2010**, *114*, 3888–3895. [[CrossRef](#)]
29. Lu, Z.; Cheng, Y.; Li, S.; Yang, Z.; Wu, R. CO<sub>2</sub> thermoreduction to methanol on the MoS<sub>2</sub> supported single Co atom catalyst: A DFT study. *Appl. Sur. Sci.* **2020**, *528*, 147047. [[CrossRef](#)]
30. Li, H.; Wang, L.; Dai, Y.; Pu, Z.; Lao, Z.; Chen, Y.; Wang, M.; Zheng, X.; Zhu, J.; Zhang, W.; et al. Synergetic interaction between neighbouring platinum monomers in CO<sub>2</sub> hydrogenation. *Nat. Nanotechnol.* **2018**, *13*, 411–417. [[CrossRef](#)]
31. Hu, J.; Yu, L.; Deng, J.; Wang, Y.; Cheng, K.; Ma, C.; Zhang, Q.; Wen, W.; Yu, S.; Pan, Y.; et al. Sulfur vacancy-rich MoS<sub>2</sub> as a catalyst for the hydrogenation of CO<sub>2</sub> to methanol. *Nat. Catal.* **2021**, *4*, 242–250. [[CrossRef](#)]
32. Han, H.; Cui, P.P.; Xiao, L.F.; Wu, W. MoCS@NSC with interfacial heterojunction nanostructure: A highly selective catalyst for synthesizing methanol from CO<sub>2</sub> at low temperature. *J. Environ. Chem. Eng.* **2021**, *9*, 106354. [[CrossRef](#)]
33. Panigrahi, P.K.; Pathak, A. Aqueous medium synthesis route for randomly stacked molybdenum disulfide. *J. Nanoparticl.* **2013**, *2013*, 671214. [[CrossRef](#)]
34. Xia, Y.; Zhu, Y.; Tang, Y. Preparation of sulfur-doped microporous carbons for the storage of hydrogen and carbon dioxide. *Carbon* **2012**, *50*, 5543–5553. [[CrossRef](#)]

35. Djamil, J.; Segler, S.A.; Dabrowski, A.; Bensch, W.; Lotnyk, A.; Schürmann, U.; Kienle, L.; Hansen, S.; Bewerie, T. The influence of carbon content on the structure and properties of MoS<sub>x</sub>C<sub>y</sub> photocatalysts for light-driven hydrogen generation. *Dalton Trans.* **2013**, *42*, 1287–1292. [[CrossRef](#)]
36. Tsai, C.; Abild-Pedersen, F.; Nørskov, J.K. Tuning the MoS<sub>2</sub> edge-site activity for hydrogen evolution via support interactions. *Nano Lett.* **2014**, *14*, 1381–1387. [[CrossRef](#)]
37. Hinnemann, B.; Moses, P.G.; Bonde, J.; Jørgensen, K.P.; Nielsen, J.H.; Horch, S.; Chorkendorff, I.; Nørskov, J.K. Biomimetic hydrogen evolution: MoS<sub>2</sub> nanoparticles as catalyst for hydrogen evolution. *J. Am. Chem. Soc.* **2005**, *127*, 5308–5309. [[CrossRef](#)]
38. Prins, R.; De Beer, V.H.J.; Somorjai, G.A. Structure and function of the catalyst and the promoter in Co-Mo Hydrodesulfurization catalysts. *Catal. Rev.* **1989**, *31*, 1–41. [[CrossRef](#)]
39. Gao, S.; Yang, L.; Shao, J.; Qu, Q.; Wu, Y.; Holze, R. Construction of hierarchical hollow MoS<sub>2</sub>/carbon microspheres for enhanced lithium storage performance. *J. Electrochem. Soc.* **2020**, *167*, 100525. [[CrossRef](#)]
40. Cao, H.; Wang, H.; Huang, Y.; Sun, Y.; Shi, S.; Tang, M. Quantification of gold(III) in solution and with a test stripe via the quenching of the fluorescence of molybdenum disulfide quantum dots. *Microchim. Acta* **2016**, *184*, 91–100. [[CrossRef](#)]
41. Zhang, J.; Cui, P.; Gu, Y.; Wu, D.; Tao, S.; Qian, B.; Chu, W.; Song, L. Encapsulating carbon-coated MoS<sub>2</sub> nanosheets within a nitrogen-doped graphene network for high-performance potassium-ion storage. *Adv. Mater. Interfaces* **2019**, *6*, 1901066. [[CrossRef](#)]
42. Zhang, X.; Ma, T.; Fang, T.; Gao, Y.; Gao, S.; Wang, W.; Liao, L. A novel MoS<sub>2</sub>@C framework architecture composites with three-dimensional cross-linked porous carbon supporting MoS<sub>2</sub> nanosheets for sodium storage. *J. Alloy. Compd.* **2020**, *818*, 152821. [[CrossRef](#)]
43. Cai, Y.; Yang, H.; Zhou, J.; Luo, Z.; Fang, G.; Liu, S.; Pan, A.; Liang, S. Nitrogen-doped hollow MoS<sub>2</sub>/C nanospheres as anode for long-life sodium-ion batteries. *Chem. Eng. J.* **2017**, *327*, 522–529. [[CrossRef](#)]
44. Hu, R.; Fang, Y.; Zhu, K.; Yang, X.; Yin, J.; Ye, K.; Yan, J.; Cao, D.; Wang, G. Carbon coated MoS<sub>2</sub> Hierarchical Microspheres enabling fast and durable potassium ion storage. *Appl. Sur. Sci.* **2021**, *564*, 150387. [[CrossRef](#)]
45. Zhao, Z.; Qin, F.; Kasiraju, S.; Xie, L.; Alam, M.K.; Chen, S.; Wang, D.; Ren, Z.; Wang, Z.; Grabow, L.C.; et al. Vertically aligned MoS<sub>2</sub>/Mo<sub>2</sub>C hybrid nanosheets grown on carbon paper for efficient electrocatalytic hydrogen evolution. *ACS Catal.* **2017**, *7*, 7312–7318. [[CrossRef](#)]
46. Lin, Q.; Dong, X.; Wang, Y.; Zheng, N.; Zhao, Y.; Xu, W.; Ding, T. Molybdenum disulfide with enlarged interlayer spacing decorated on reduced graphene oxide for efficient electrocatalytic hydrogen evolution. *J. Mater. Sci.* **2020**, *55*, 6637–6647. [[CrossRef](#)]
47. Yin, X.; Sun, G.; Song, A.; Wang, L.; Wang, Y.; Dong, H.; Shao, G. A novel structure of Ni-(MoS<sub>2</sub>/GO) composite coatings deposited on Ni foam under supergravity field as efficient hydrogen evolution reaction catalysts in alkaline solution. *Electrochim. Acta* **2017**, *249*, 52–63. [[CrossRef](#)]
48. Yang, S.; Wang, Y.; Zhang, H.; Zhang, Y.; Liu, L.; Fang, L.; Yang, X.; Gu, X.; Wang, Y. Unique three-dimensional Mo<sub>2</sub>C@MoS<sub>2</sub> heterojunction nanostructure with S vacancies as outstanding all-pH range electrocatalyst for hydrogen evolution. *J. Catal.* **2019**, *371*, 20–26. [[CrossRef](#)]
49. Tang, Y.; Wang, Y.; Wang, X.; Li, S.; Huang, W.; Dong, L.; Liu, C.; Li, Y.; Lan, Y. Molybdenum disulfide/nitrogen-doped reduced graphene oxide nanocomposite with enlarged interlayer spacing for electrocatalytic hydrogen evolution. *Adv. Energy Mater.* **2016**, *6*, 1600116. [[CrossRef](#)]
50. Liu, H.; Hu, H.; Wang, J.; Niehoff, P.; He, X.; Paillard, E.; Eder, D.; Winter, M.; Li, J. Hierarchical ternary MoO<sub>2</sub>/MoS<sub>2</sub>/heteroatom-doped carbon hybrid materials for high-performance lithium-ion storage. *ChemElectroChem* **2016**, *3*, 922–932. [[CrossRef](#)]
51. Ma, Y.; Wang, J.; Goodman, K.R.; Head, A.R.; Tong, X.; Stacchiola, D.J.; White, M.G. Reactivity of a zirconia-copper inverse catalyst for CO<sub>2</sub> hydrogenation. *J. Phys. Chem. C* **2020**, *124*, 22158–22172. [[CrossRef](#)]
52. Gao, P.; Li, F.; Zhan, H.J.; Zhao, N.; Xiao, F.K.; Wei, W.; Zhong, L.S.; Wang, H.; Sun, Y.H. Influence of Zr on the performance of Cu/Zn/Al/Zr catalysts via hydrotalcite-like precursors for CO<sub>2</sub> hydrogenation to methanol. *J. Catal.* **2013**, *298*, 51–60. [[CrossRef](#)]
53. Xiao, J.; Mao, D.S.; Guo, X.M.; Yu, J. Effect of TiO<sub>2</sub>, ZrO<sub>2</sub>, and TiO<sub>2</sub>-ZrO<sub>2</sub> on the performance of CuO-ZnO catalyst for CO<sub>2</sub> hydrogenation to methanol. *Appl. Surf. Sci.* **2015**, *338*, 146–153. [[CrossRef](#)]
54. Liu, T.; Xu, D.; Wu, D.; Liu, G.; Hong, X. Spinel ZnFe<sub>2</sub>O<sub>4</sub> regulates copper sites for CO<sub>2</sub> hydrogenation to methanol. *ACS Sustain. Chem. Eng.* **2021**, *9*, 4033–4041. [[CrossRef](#)]
55. Kiciński, W.; Szala, M.; Bystrzejewski, M. Sulfur-doped porous carbons: Synthesis and applications. *Carbon* **2014**, *68*, 1–32. [[CrossRef](#)]
56. Posada-Pérez, S.; Ramírez, P.J.; Gutiérrez, R.A.; Stacchiola, D.J.; Viñes, F.; Liu, P.; Illas, F.; Rodríguez, J.A. The conversion of CO<sub>2</sub> to methanol on orthorhombic β-Mo<sub>2</sub>C and Cu/β-Mo<sub>2</sub>C catalysts: Mechanism for admetal induced change in the selectivity and activity. *Catal. Sci. Technol.* **2016**, *6*, 6766–6777. [[CrossRef](#)]
57. Posada-Pérez, S.; Viñes, F.; Rodríguez, J.A.; Illas, F. Fundamentals of methanol synthesis on metal carbide based catalysts: Activation of CO<sub>2</sub> and H<sub>2</sub>. *Top. Catal.* **2015**, *58*, 159–173. [[CrossRef](#)]
58. Posada-Pérez, S.; Politi, J.R.d.S.; Vines, F.; Illas, F. Methane capture at room temperature: Adsorption on cubic δ-MoC and orthorhombic β-Mo<sub>2</sub>C molybdenum carbide (001) surfaces. *RSC Adv.* **2015**, *5*, 33737–33746. [[CrossRef](#)]
59. Alves, L.M.N.C.; Almeida, M.P.; Ayala, M.; Watson, C.D.; Jacobs, G.; Rabelo-Neto, R.C.; Noronha, F.B.; Mattos, L.V. CO<sub>2</sub> methanation over metal catalysts supported on ZrO<sub>2</sub>: Effect of the nature of the metallic phase on catalytic performance. *Chem. Eng. Sci.* **2021**, *239*, 116604. [[CrossRef](#)]

60. Yu, J.; Yang, M.; Zhang, J.; Ge, Q.; Zimina, A.; Pruessmann, T.; Zheng, L.; Grunwaldt, J.D.; Sun, J. Stabilizing Cu<sup>+</sup> in Cu/SiO<sub>2</sub> catalysts with a shattuckite-like structure boosts CO<sub>2</sub> hydrogenation into methanol. *ACS Catal.* **2020**, *10*, 14694–14706. [[CrossRef](#)]
61. Zhao, K.; Wang, L.; Moiola, E.; Calizzi, M.; Züttel, A. Identifying reaction species by evolutionary fitting and kinetic analysis: An example of CO<sub>2</sub> hydrogenation in DRIFTS. *J. Phys. Chem. C* **2021**, *123*, 8785–8792. [[CrossRef](#)]
62. Fisher, I.A.; Bell, A.T. In situ infrared study of methanol synthesis from H<sub>2</sub>/CO over Cu/SiO<sub>2</sub> and Cu/ZrO<sub>2</sub>/SiO<sub>2</sub>. *J. Catal.* **1998**, *178*, 153–173. [[CrossRef](#)]
63. Fisher, I.A.; Bell, A.T. In-situ infrared study of methanol synthesis from H<sub>2</sub>/CO<sub>2</sub> over Cu/SiO<sub>2</sub> and Cu/ZrO<sub>2</sub>/SiO<sub>2</sub>. *J. Catal.* **1997**, *172*, 222–237. [[CrossRef](#)]
64. Xu, M.; Yao, S.; Rao, D.; Niu, Y.; Liu, N.; Peng, M.; Zhai, P.; Man, Y.; Zheng, L.; Wang, B.; et al. Insights into interfacial synergistic catalysis over Ni@TiO<sub>2-x</sub> catalyst toward Water-Gas shift reaction. *J. Am. Chem. Soc.* **2018**, *140*, 11241–11251. [[CrossRef](#)]
65. Cerdá-Moreno, C.; Chica, A.; Keller, S.; Rautenberg, C.; Bentrup, U. Ni-sepiolite and Ni-todorokite as efficient CO<sub>2</sub> methanation catalysts: Mechanistic insight by operando DRIFTS. *Appl. Catal. B Environ.* **2020**, *264*, 118546. [[CrossRef](#)]
66. Malik, A.S.; Zaman, S.F.; Al-Zahrani, A.A.; Daous, M.A.; Driss, H.; Petrov, L.A. Selective hydrogenation of CO<sub>2</sub> to CH<sub>3</sub>OH and in-depth DRIFT analysis for PdZn/ZrO<sub>2</sub> and CaPdZn/ZrO<sub>2</sub> catalysts. *Catal. Today* **2020**, *357*, 573–582. [[CrossRef](#)]
67. Luo, L.; Wang, M.; Cui, Y.; Chen, Z.; Wu, J.; Cao, Y.; Luo, J.; Dai, Y.; Li, W.; Bao, J.; et al. Surface iron species in palladium-iron intermetallic nanocrystals that promote and stabilize CO<sub>2</sub> methanation. *Angew. Chem. Int. Ed.* **2020**, *59*, 14434–14442. [[CrossRef](#)]
68. Kattel, S.; Yan, B.; Yang, Y.; Chen, J.G.; Liu, P. Optimizing binding energies of key intermediates for CO<sub>2</sub> hydrogenation to methanol over oxide-supported copper. *J. Am. Chem. Soc.* **2016**, *138*, 12440–12450. [[CrossRef](#)]
69. Romero-Sarria, F.; Bobadilla, L.F.; Barrera, E.M.J.; Odriozola, J.A. Experimental evidence of HCO species as intermediate in the fischer tropesch reaction using operando techniques. *Appl. Catal. B Environ.* **2020**, *272*, 119032. [[CrossRef](#)]
70. Wang, X.; Zhang, Y.; Si, H.; Zhang, Q.; Wu, J.; Gao, L.; Wei, X.; Sun, Y.; Liao, Q.; Zhang, Z.; et al. Single-atom vacancy defect to trigger high-efficiency hydrogen evolution of MoS<sub>2</sub>. *J. Am. Chem. Soc.* **2020**, *142*, 4298–4308. [[CrossRef](#)]
71. Mu, X.; Zhu, Y.; Gu, X.; Dai, S.; Mao, Q.; Bao, L.; Li, W.; Liu, S.; Bao, J.; Mu, S. Awakening the oxygen evolution activity of MoS<sub>2</sub> by exophilic-metal induced surface reorganization engineering. *J. Energy Chem.* **2021**, *62*, 546–551. [[CrossRef](#)]
72. Gong, F.; Ye, S.; Liu, M.; Zhang, J.; Gong, L.; Zeng, G.; Meng, E.; Su, P.; Xie, K.; Zhang, Y.; et al. Boosting electrochemical oxygen evolution over yolk-shell structured O-MoS<sub>2</sub> nanoreactors with sulfur vacancy and decorated Pt nanoparticles. *Nano Energy* **2020**, *78*, 105284. [[CrossRef](#)]
73. Liu, G.; Robertson, A.W.; Li, M.M.; Kuo, W.C.H.; Darby, M.T.; Muhieddine, M.H.; Lin, Y.C.; Suenaga, K.; Stamatakis, M.; Warner, J.H.; et al. MoS<sub>2</sub> monolayer catalyst doped with isolated Co atoms for the hydrodeoxygenation reaction. *Nat. Chem.* **2017**, *9*, 810–816. [[CrossRef](#)]
74. Cai, L.; He, J.; Liu, Q.; Yao, T.; Chen, L.; Yan, W.; Hu, F.; Jiang, Y.; Zhao, Y.; Hu, T.; et al. Vacancy-induced ferromagnetism of MoS<sub>2</sub> nanosheets. *J. Am. Chem. Soc.* **2015**, *137*, 2622–2627. [[CrossRef](#)] [[PubMed](#)]